J Mater Sci (2023) 58:9737–9754

Metals & corrosion

Dissimilar friction stir welding of 2219-T8 and 2195-T8 aluminum alloys: part I—microstructure evolution and mechanical properties

Zhenlin Wang[1,2], Wenli Zhu[3], Zhen Zhang[1,2,*], Beibei Wang[1], Peng Xue[1,2], Dingrui Ni[1,2,*], Fengchao Liu[1], Bolv Xiao[1,2], Zongyi Ma[1,2], Feifan Wang[3], and Weidong Zheng[3]

[1] *Shi-Changxu Innovation Center for Advanced Materials, Institute of Metal Research, Chinese Academy of Science, Shenyang 110016, China*

[2] *School of Materials Science and Engineering, University of Science and Technology of China, 72 Wenhua Road, Shenyang 110016, China*

[3] *China Academy of Launch Vehicle Technology, Beijing 100076, China*

Received: 15 February 2023

Accepted: 24 May 2023

ABSTRACT

The need for 2219 aluminum alloy and 2195 Al–Li alloy dissimilar friction stir welding (FSW) arises as the conventional 2219Al alloy was gradually replaced by the novel 2195Al alloy in fabrication of fuel tanks. However, the systematic investigation about the effect of welding parameters and material positioning on the microstructure evolution and mechanical properties of dissimilar FSW 2219Al/2195Al joints is lacking. In the present study, 2219Al-T8/2195Al-T8 plates were subjected to FSW under rotation rates of 800–1200 rpm and welding speeds of 200–800 mm min^{-1} with placing 2219Al-T8 alloys on the advancing side (AS) and retreating side (RS), respectively. The results showed that sound FSW joints were obtained under all the welding conditions. Welding parameters and material positioning affected the joint strength and fracture failure behavior. The FSW thermal cycle resulted in low hardness zones (LHZs) on both the 2219Al-T8 and 2195Al-T8 sides. The LHZ on the 2219Al-T8 side, characterized by partial coarsening of θ' (Al_2Cu) precipitates and dissolution of the residual precipitates, showed the minimum hardness in the entire FSW joints. When 2219Al-T8 alloy was placed on the AS, the LHZ on the 2219Al-T8 side experienced higher peak temperature, and therefore more dissolution of θ' than that on the RS, thereby obtaining higher tensile strength. The tensile strength of the FSW joints at room temperature and − 196 °C largely increased as the welding speed increased from 200 to 400 mm min^{-1}. The FSW joints presented much higher tensile strength at − 196 °C than that at room temperature under the

---

Handling Editor: P. Nash.

Address correspondence to E-mail: zhangzhen@imr.ac.cn; drni@imr.ac.cn

https://doi.org/10.1007/s10853-023-08637-7

identical welding parameters and material position. The FSW joints fractured along the LHZ on the 2219Al-T8 side during tension. For the bending testing, the up and down bending failure angles were about 91–117° and 88–109°, respectively, with the weak zone appearing in “S” line or HAZ on the 2195Al-T8 side.

Abbreviations

FSW	Friction stir welding
BM	Base material
NZ	Nugget zone
TMAZ	Thermal-mechanically affected zone
HAZ	Heat affected zone
SDZ	Shoulder driven zone.
PDZ	Pin-driven zone
SWZ	Swirl zone (SWZ)
DIC	Digital image correlation
TEM	Transmission electron microscopy
SEM	Scanning electron microscopy
YS	Yield strength
UTS	Ultimate tensile strength
EL	Elongation
AS	Advancing side
RS	Retreating side

Introduction

The conventional 2219 aluminum (2219Al) alloy is being gradually replaced by the novel 2195 aluminum–lithium (2195Al) alloy with excellent strength and low density in fabrication of fuel tanks [1, 2]. Therefore, the joining between the dissimilar 2219Al and 2195Al alloys is indispensable [3]. However, fusion welding of the 2219Al and 2195Al alloys is inadvisable because of the poor weldability issues like branch crystal, segregation, porosity and Li element evaporation [4, 5]. Friction stir welding (FSW) characterized by solid state forming is considered to be an alternative welding technology for the 2219Al and 2195 Al alloys [2].

In recent years, dissimilar aluminum alloys have been subjected to extensive FSW investigations [6–10], and most investigations showed that the weak zone was on the soft material side of the FSW dissimilar aluminum alloys. The positioning (advancing side (AS) or retreating side (RS)) of the soft material played a significant role in the joint quality and mechanical properties for FSW dissimilar aluminum alloys. The FSW investigations of 7039Al-T6/2024Al-T3 [6], 7075Al-T6/2024Al-T3 [7], 7075Al-T6/6061Al-T6 [8], 6082Al-T6/7075Al-T651 [9] and 6082Al-T6/2024Al-T3 [10] showed that placing the softer aluminum alloys on the AS could obtain higher joint tensile strength for FSW dissimilar precipitation-hardened aluminum alloys. However, the detailed microstructure evolution mechanism explanation was absent.

Recently, Fang et al. [11] reported that 2-mm-thick sound FSW 2219Al-T87/2195Al-T8 joints were obtained under welding speeds of 100–500 mm min^{-1} for a constant rotation rate of 1000 rpm. It was shown that whether 2219Al-T87 or 2195Al-T8 alloys were positioned on the AS had no obvious effect on the tensile strength of the joint and the welding speed did not influence the tensile strength, with the tensile fracture location being located at the nugget zone (NZ) or NZ/thermo-mechanically affected zone (TMAZ) interface. Wang et al. [12] reported that for 2-mm-thick sound FSW 2219Al-T87/2195Al-T8 joints with 2219Al-T87 alloy on the AS, the tensile strength increased with increasing the welding speed from 100 to 200 mm min^{-1} but decreased as the welding speed further increased from 200 to 400 mm min^{-1}, with the fracture occurring at the NZ or NZ/TMAZ interface. However, Agilan et al. [13] reported that for 6-mm-thick sound FSW 2219Al-T8/2195Al-T8 joints under 800 rpm–300 mm min^{-1}, the tensile strength of the dissimilar joint was marginally higher than that of the 2219 similar joint, and the failure location was located at the TMAZ on the 2219 side; furthermore, the tensile strength of the joint with the 2219Al-T8 on the AS was about 17 MPa higher than that with the 2219Al-T8 on the RS. These investigations indicated that the better material positioning, relationship between the welding parameters and tensile strength, and fracture location remain controversial for dissimilar FSW 2219Al/2195Al joints.

For FSW precipitation-hardened aluminum alloys [14, 15], it is reported that the joint strength increased with increasing the welding speed and was independent of the rotation rate. For example, Zhang et al. [16, 17] reported that for 5.4-mm-thick FSW 2219-T6 joints under rotation rates of 400–1200 rpm and welding speeds of 100–800 mm min^{-1}, the tensile strength of the joints increased with the increase in the welding speed and was independent of the rotation rate. For aluminum–lithium alloys, however, Tao et al. [18] and Zhang et al. [19] reported that for the 2.0-mm-thick FSW 2060-T8 and 2.5-mm-thick FSW 2195Al-T8 joints, the joint strength increased as the welding speed increased, while for a 5-mm-thick 2195-T8 alloy, the tensile strength was improved by increasing the rotation rates from 700 to 1300 rpm [20], and a similar result was obtained for FSW of 2198Al-T8 alloy [21].

Clearly, the joint strength of 2219 and Al-Li alloys exhibited different welding parameter dependences. How the welding parameters affect the joint strength of dissimilar 2219/2195 FSW joints has not been well understood due to very limited investigations [11, 12]. Furthermore, for 6-mm-thick FSW dissimilar joints of 2219Al-T8/2195Al-T8 alloys that are needed for the fabrication of fuel tanks, only a welding parameter of 800 rpm–300 mm min^{-1} was investigated [13]. The effect of FSW parameters on the joint strength is still unclear.

The fuel tanks contain dome and barrel structures with straight and ring welds [2]. It is necessary to evaluate the bending performance of the FSW. However, for the FSW dissimilar aluminum alloy joints, only FSW 6101Al-T6/6351Al-T6 joint was subjected to bending evaluation [22]. The investigation of the bending performance of the FSW 2219Al/2195Al joint is still lacking.

Under ideal laboratory conditions with the appropriate welding tools and parameters, the sound FSW joints could be easily achieved for 2–8-mm-thick precipitation-hardened aluminum alloy plates [7–21]; however, welding defects may arise in the industrial production of the huge fuel tanks [23]. Therefore, it is necessary to repair the welding defects of fuel tanks produced by FSW. However, the repair welding of dissimilar FSW joints of 2219Al-T8 and 2195Al-T8 aluminum alloys has not been reported so far.

In this study, 6-mm-thick plates of 2219Al-T8 and 2195Al-T8 alloys were subjected to (a) FSW investigation at rotation rates of 800–1200 rpm and welding speeds of 200–800 mm min^{-1}, with the aim of revealing the intrinsic relationship between material positioning, welding parameters, temperature distribution, microstructure, mechanical properties and failure behavior of the FSW 2219Al-T8/2195Al-T8 joints, and (b) multi-pass repair welding based on initial FSW under optimized welding parameters and material position to study the effect of repair welding on the microstructure, mechanical properties and fracture behavior of FSW 2219Al/2195Al joints. (a) Is presented in this article, while (b) will be described in the other article.

Materials and experiment procedures

6-mm-thick rolled 2219Al-T8 and 2195Al-T8 alloy plates were used in this study. The chemical composition and mechanical properties of the base materials (BMs) are shown in Tables 1 and 2, respectively. The plates, with a length of 300 mm and a width of 100 mm, were cleared by abrasive papers on the top surfaces and butt surfaces, and then butt welded across the rolling direction under plunge depths of 0.05–0.15 mm rotation rates of 800–1200 rpm and welding speeds of 200–800 mm min^{-1} (Table 3), using a FSW machine with 2.75° tilt angle. A H13 steel tool with a concave shoulder 21 mm in diameter and a threaded cylindrical pin 8 mm in diameter and 5.8 mm in length was used.

In order to study the effect of material positioning on tensile properties of the FSW joints, 2219Al-T8 alloy plate was positioned on the AS and RS during FSW, respectively. The FSW joints were designated in brief forms. For example, joint 2219RS-800-200 denotes the joint welded at a rotation rate of 800 rpm and a welding speed of 200 mm min^{-1} with the 2219Al-T8 alloy plates being positioned on the RS (Table 3). All the FSW joints were naturally aged at room temperature (20 °C) for more than 7 days before the microstructural examination and property evaluation.

All the joints were cross-sectioned perpendicular to the welding direction using an electrical discharge machine at positions more than 40 mm away from the starting point of the joints. Metallographic

Table 1 Chemical compositions of 2219Al-T8 and 2195Al-T8 rolled plates (wt%)

Alloy	Chemical composition (wt%)									
	Cu	Mg	Li	Ag	Zr	Mn	Fe	Si	Zn	Ti	Al
2219Al	5.8–6.8	0.02	–	–	–	0.2–0.4	0.2	0.2	0.1	0.1–0.2	Bal
2195Al	3.7–4.3	0.25–0.8	0.8–1.2	0.25–0.6	0.08–0.1	0.25	0.15	0.12	–	0.1	Bal

Table 2 Tensile properties of 2219Al-T8 and 2195Al-T8 rolled plates

Alloy	Temperature, °C	Tensile properties		
		YS, MPa	UTS, MPa	EI, %
2219Al-T8	20	383 ± 2.1	462 ± 0.6	14.7 ± 0.6
	− 196	442 ± 3.0	572 ± 1.0	14.5 ± 0.0
2195Al-T8	20	553 ± 2.5	581 ± 3.5	13.8 ± 0.3
	− 196	632 ± 19.2	714 ± 20.6	13.3 ± 1.3

Table 3 Welding parameters of FSW 2219Al-T8/2195Al-T8 joints

Number	Material position	Rotation rate, rpm	Welding speed, mm min^{-1}	Plunge depth, mm	Designation
1	2219RS	800	200	0.05	2219RS-800-200
2	2219RS	800	400	0.10	2219RS-800-400
3	2219AS	800	200	0.05	2219AS-800-200
4	2219AS	800	400	0.10	2219AS-800-400
5	2219AS	1200	800	0.15	2219AS-1200-800

observation was carried out via a Leica DMI optical microscope (OM). For observing the grain structure, the polished cross sections of the joints were chemically etched by the Keller reagent (2 mL HF + 3 mL HCl + 5 mL HNO_3 + 190 mL H_2O). Furthermore, in order to observe the distribution of the "S" line, the joints were etched with 10% NaOH solution for 30 min and were then wiped with wet cotton ball.

Vickers microhardness of the joints was measured on the cross section of the joints perpendicular to the welding direction using an automatic Leco-LM-247AT hardness tester under a load of 500 g with a holding time of 13 s. The hardness profiles of the joints were obtained along the mid-thickness of the cross section at an interval of 1 mm. The hardness intensity maps were acquired by measuring 5 lines on the cross section with the interval of 1 mm. In each of the lines, 23 indentations with a 1-mm spacing interval were measured. After the LHZs were obtained, the thermocouples were embedded in the LHZs at the middle position of the plate thickness to record the temperature history of the dissimilar FSW 2219Al-T8/2195Al-T8 process. The temperature data were sampled at an interval of 0.02 s by a temperature recorder.

In order to obtain the real mechanical properties and fracture locations of the joints, the joint surfaces

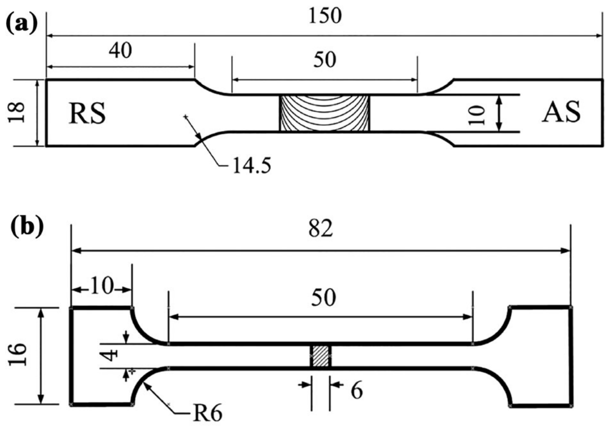

Dimensions in mm

Figure 1 Configuration and sizes of tensile specimens of **a** at room temperature and **b** at − 196 °C.

for the tensile specimens were planned with abrasive papers to insure the equal cross-sectional area at various locations of the joints. Figure 1 shows the configuration and size of the transverse tensile specimens, i.e., the room temperature (RT) tensile specimen with a width of 10 mm and the low temperature (− 196 °C) tensile specimen with a width of 4 mm. Three specimens were tested for each set of FSW joints at a strain rate of 1.0×10^{-3} s^{-1}, using a Zwick–Roell tensile machine at RT and − 196 °C, respectively. Digital image correlation (DIC) was adopted to analyze the evolution of the strain fields during tensile testing. In this work, two high-speed cameras with Schneider 50 mm f/3D lens were used to capture the upper surface of the joint, and the acquisition frequency was consistent with five images per second. A DIC software of PMLAB was used to capture the local displacement fields of the dissimilar FSW joint. To track regions on the sample surface, the speckle pattern was carried out using round dot of black spray paint over the white base paint.

The bending specimen, with a length of 150 mm and a width of 120 mm, were tested using three-point bending test at a velocity of 10 mm min^{-1}. Tension stress occurred at the top part during up bending, while the bottom part suffered tension stress during down bending for the FSW joint.

Distribution of precipitates at the varied zones was characterized using transmission electron microscopy (TEM, FEI-T20). TEM and electron backscattered diffraction (EBSD) specimens were cut from corresponding locations in the welds using an electrical-discharge machine. The TEM specimens were thinned down to 60–70 μm with waterproof abrasive paper, were then punched into rounds pieces of 3 mm in diameter with eyelet machine, and were finally prepared by a twin jet polishing machine with a solution of 25% methanol and 75% nitric acid at the condition of − 25 to − 30 °C below freezing and 12 V. The prepared EBSD samples were electrolytic polished by 10% of perchloric acid alcohol solution at the condition of −25 to − 30 °C below freezing and 12 V.

Results and discussion

Macrostructure and material flow

Figure 2 shows the surficial morphologies of the FSW 2219Al-T8/2195Al-T8 joints under varied material positions and welding parameters. It can be seen that all the joint surfaces were basically smooth and no obvious macroscopic surface defects were observed (Fig. 2a–e).

Figure 3 shows the cross-sectional macrostructures of the FSW 2219Al-T8/2195Al-T8 joints. No welding defect was detected in the FSW joints. Three subzones; i.e., NZ, TMAZ, and HAZ, were discernible (Fig. 3a). Based on the characteristics of material flow and the role of shoulder and pin in the formation of the NZ, the NZ can be subdivided into three subzones: the shoulder-driven zone (SDZ), the pin-driven zone (PDZ) [24] and the swirl zone (SWZ) [25]. The onion rings were located at the PDZ. At a rotation rate of 800 rpm, increasing the welding speed from 200 to 400 mm min^{-1} resulted in the shrinking of the SDZ, enlarging of the PDZ and incomplete forming of the onion rings. The shapes of the SDZ and PDZ (onion rings included) were apparently affected by the rotation rate and welding speed, and the material positioning exerted little influence on the size of SDZ, PDZ and SWZ (Fig. 3a–e).

In order to reveal the effect of material positioning and welding parameters on the material flow during the FSW 2219Al-T8/2195Al-T8 process, the cross-sectional macroscopic patterns of “S” line (partially marked by black arrows) of the joints are shown in Fig. 4. The “S” line, derived from the broken oxides on the butting surfaces, appeared in the NZ and reflected the material flow characteristics during FSW. Generally, the “S” line showed a zigzag pattern. The “S” lines of joints 2219RS-800-200 and 2219AS-800-200 showed the similar pattern at the lower and middle parts. The “S” line started from the bottom of the weld center-line, deviated upwards to the AS at the lower part (SWZ), then extended to the RS along the interface of PDZ and TMAZ at the middle part. However, at the upper part the “S” line vertically moved up to the joint surface for joint 2219RS-800-200 but extended toward to the RS for joint 2219AS-800-200. This indicated that the material positioning mainly affected the material flow at the upper part of the NZ under 800 rpm–200 mm min^{-1} (Fig. 4a, b).

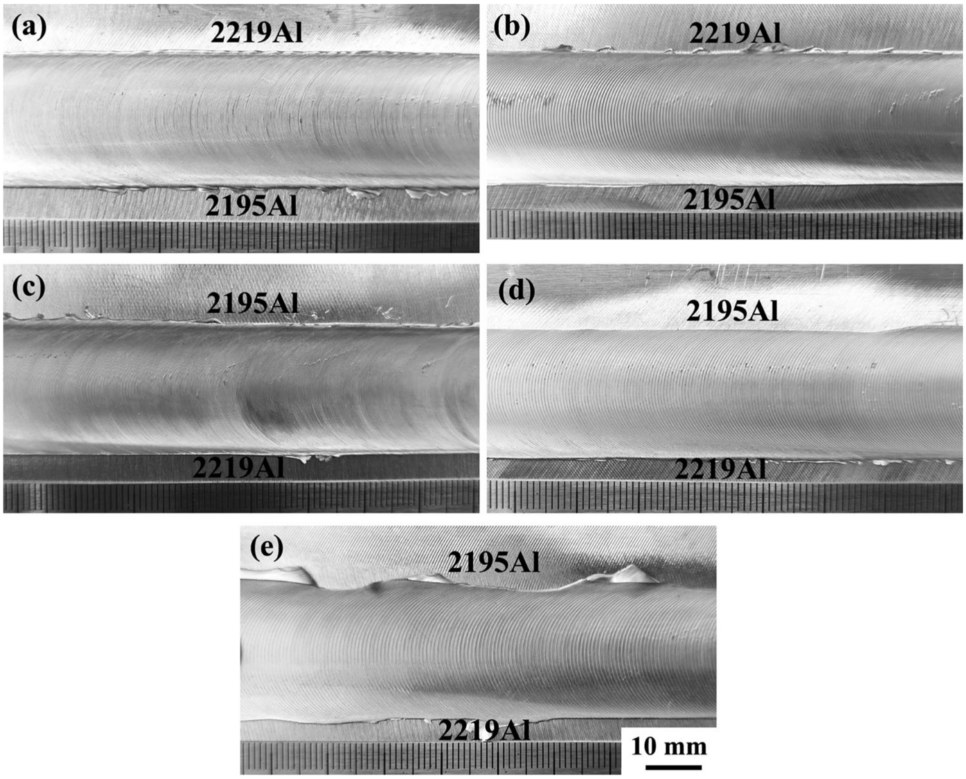

Figure 2 Surface morphologies of FSW 2219Al-T8/2195Al-T8 joints: **a** 2219RS-800-200, **b** 2219RS-800-400, **c** 2219AS-800-200, **d** 2219AS-800-400, and **e** 2219AS-1200-800.

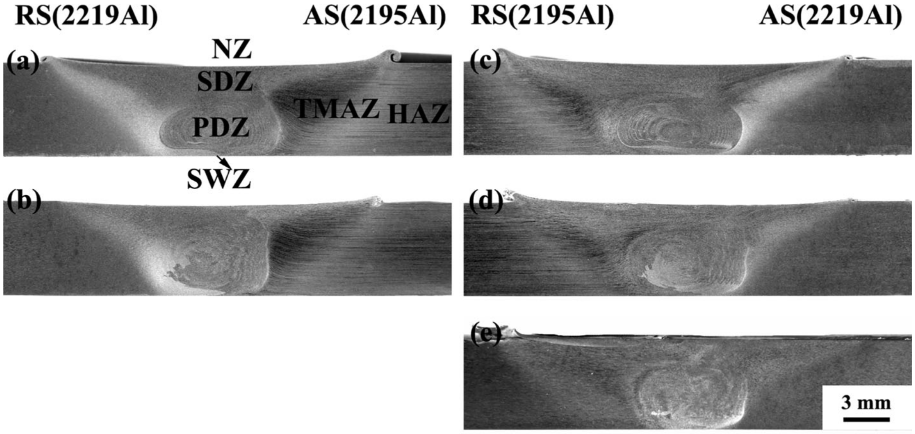

Figure 3 Cross-sectional macrostructure of FSW 2219Al-T8/2195Al-T8 joints: **a** 2219RS-800-200, **b** 2219RS-800-400, **c** 2219AS-800-200, **d** 2219AS-800-400, and **e** 2219AS-1200-800.

At a rotation rate of 800 rpm, increasing the welding speed from 200 to 400 mm min^{-1} led to less tortuous "S" lines in joints 2219RS-800-400 and 2219AS-800-400 compared with that of joints 2219RS-800-200 and 2219AS-800-200. The "S" line of joint 2219AS-1200-800 became further less tortuous compared to that of joint 2219AS-800-400.

Hardness distribution

Figure 5 shows the microhardness profiles of the FSW 2219Al-T8/2195Al-T8 joints. For facilitating comparison, 2195Al-T8 and 2219Al-T8 alloys are placed on the left and right sides of Fig. 5, respectively. In order to accurately determine the hardness distribution, the positions and values of the LHZs of FSW 2219Al-T8/2195Al-T8 joints are shown in Table 4. Generally, the microhardness of the FSW joints showed "W"-shaped pattern with the 2219Al-T8 side having lower hardness for all the joints. Five observations can be made: (a) two notable LHZs, about 6 mm and 10 mm from the centerline of the NZ, respectively, were observed on the 2219Al-T8 and 2195Al-T8 sides of each joint; (b) the hardness of

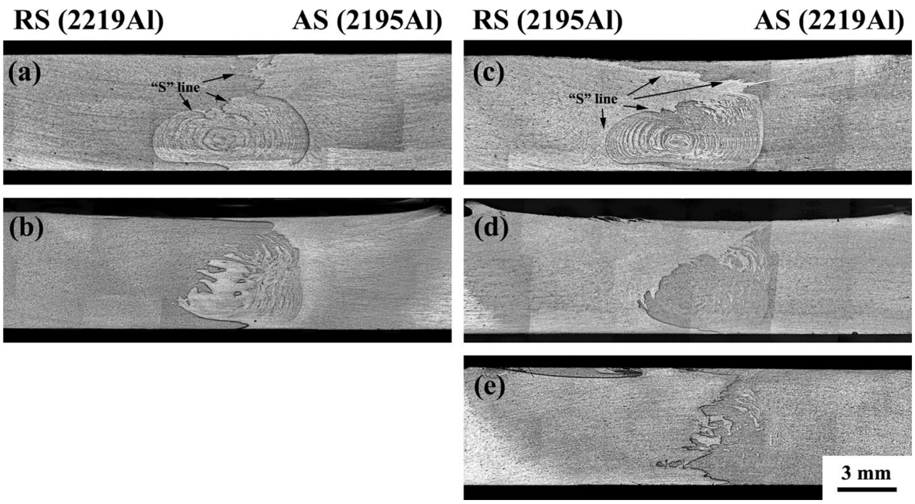

Figure 4 Cross-section morphologies of "S" line in FSW 2219Al-T8/2195Al-T8 joints: **a** 2219RS-800-200, **b** 2219RS-800-400, **c** 2219AS-800-200, **d** 2219AS-800-400, and **e** 2219AS-1200-800.

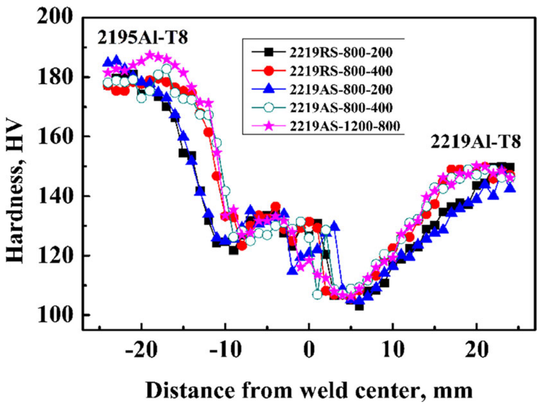

Figure 5 Microhardness profile of FSW 2219Al-T8/2195Al-T8 joints at various welding parameters and material position.

the LHZ on the 2219Al-T8 side was much lower than that on the 2195Al-T8 side; (c) increasing the welding speed from 200 to 400 mm min^{-1} resulted in the movement of the LHZ toward to the weld center and meanwhile remarkably increased the hardness of the LHZ on the 2195Al-T8 side, but only slightly increased the hardness of the LHZ on the 2219Al-T8 side; (d) the LHZs of joints 2219AS-1200-800 and 2219AS-800-400 exhibited similar hardness values; (e) The LHZs on the 2219Al-T8 side was located at the HAZs for all the FSW joints.

It is documented that the tensile properties and fracture behavior are dependent on the hardness of the LHZs for FSW precipitation-hardened aluminum alloys [14, 15, 26]. The LHZ on the 2219Al-T8 side showed the minimum hardness and deserved the additional attention for FSW 2219Al-T8/2195Al-T8 joints. In order to accurately reveal the hardness distribution and location of the LHZ on the 2219Al-T8 side, the microhardness intensity maps of the FSW 2219Al-T8/2195Al-T8 joints are shown in Fig. 6, in which 2195Al-T8 and 2219Al-T8 alloys are placed on the left and right sides, respectively, for all the FSW joints. It can be seen that the hardness of the LHZs on the 2219Al-T8 side of joints 2219AS-800-200 and 2219AS-800-400 is slightly higher than that of joints 2219RS-800-200 and 2219RS-800-400, respectively (Fig. 6a–d), indicating that placing the 2219Al-T8 alloy on the AS resulted in higher hardness in the LHZs on the 2219Al-T8 side.

The above results indicated the FSW 2219Al-T8/2195Al-T8 joints showed the lower hardness on the 2219Al-T8 side and would determine the mechanical properties and fracture behavior of the dissimilar FSW 2219Al-T8/2195Al-T8 joints. Therefore, the microstructure of the 2219Al-T8 side was subjected to detailed examinations.

Table 4 Positions and values of the LHZs of FSW 2219Al-T8/2195Al-T8 joints

Joint	Distance from the weld center, mm	Value, Hv
2219RS-800-200	6	103.1
2219RS-800-400	5	105.5
2219AS-800-200	6	104.7
2219AS-800-400	4	107.1
2219AS-1200-800	5	106.3

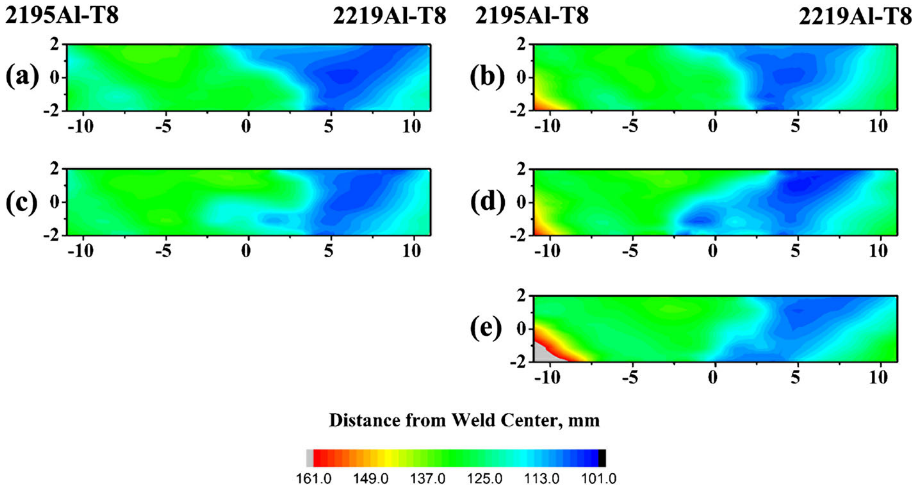

Figure 6 Microhardness intensity maps of FSW 2219Al-T8/2195Al-T8 joints: **a** 2219RS-800-200, **b** 2219RS-800-400, **c** 2219AS-800-200, **d** 2219AS-800-400, and **e** 2219AS-1200-800.

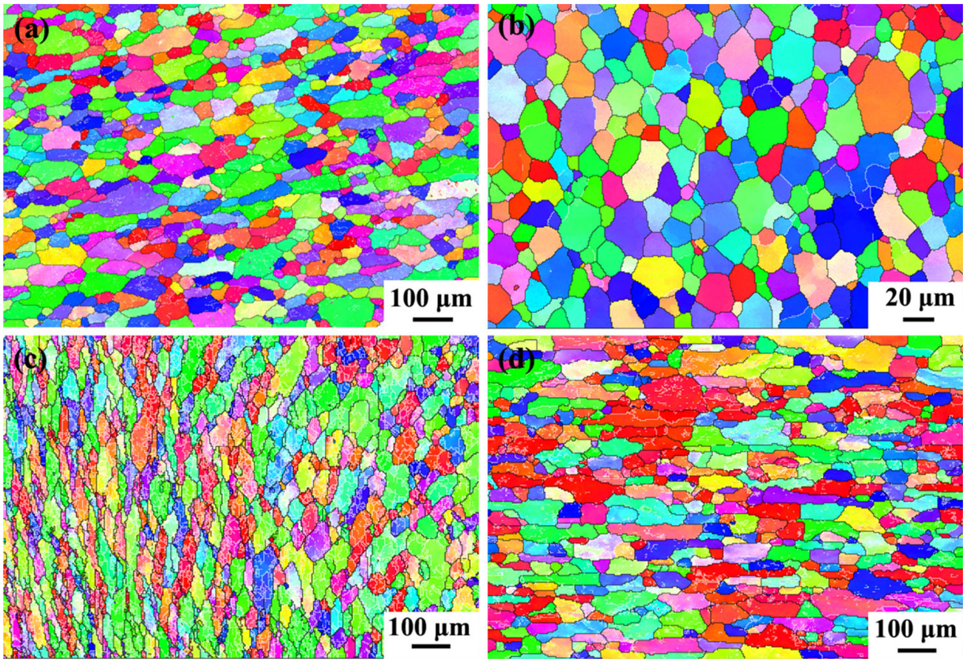

Figure 7 EBSD orientation color maps on 2219Al-T8 side of joint 2219AS-800-200: **a** 2219Al-BM, **b** NZ, **c** TMAZ, and **d** HAZ.

Microstructure

Figures 7 and 8 shows the EBSD orientation color maps and grain orientation distribution of the BM, NZ, TMAZ and HAZ on the 2219Al-T8 side of joint 2219AS-800-200. The black and white lines represent the high-angle grain boundaries (HAGBs, ≥ 15°) and low-angle grain boundaries (LAGBs, < 15°) in the images, respectively. It can be seen that the coarse and elongated grains of the 2219Al-T8 BM were about 100–200 μm in length and approximately 10–50 μm in width, which resulted from the hot-rolled process (Fig. 7a). In the NZ, the average grain size was about 15.1 μm with a high HAGB fraction accounting for 88.1% (Figs. 7b and 8b), indicating that a dynamic recrystallization occurred in the NZ. Compared to the NZ, the TMAZ experienced the weaker plastic deformation and lower heat input, leading to the deformed and elongated grains with a low HAGB fraction accounting for 34.4% (Figs. 7c and 8c). The HAZ only suffered from the thermal cycle and the grains were therefore slightly coarsened with the HAGB fraction accounting for 55.2% (Figs. 7d and 8d).

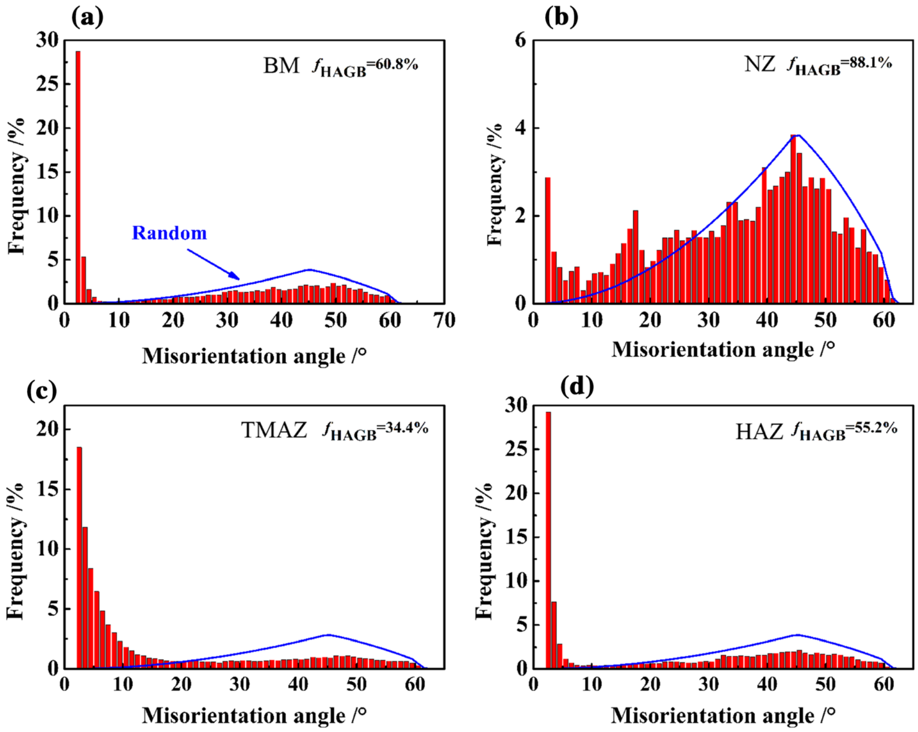

Figure 8 Grain orientation distribution on 2219Al-T8 side of joint 2219AS-800-200: **a** 2219Al-BM, **b** NZ, **c** TMAZ, and **d** HAZ.

Precipitate evolution mechanism of the joints

For precipitation-hardened aluminum alloys, the hardness distribution of the FSW joints was mainly dependent on the precipitate distribution, which was mainly determined by the temperature histories of FSW. During FSW, the varied positions of the FSW joints experienced the thermal cycles with different peak temperatures, heating rates, and cooling rates. The precipitates therefore evolved in different ways at the NZ and LHZ on the 2219Al-T8 side of the FSW 2219Al-T8/2195Al-T8 joints.

The hardness distribution of the BT-FSW 2219-T8 joints was mainly dependent on the precipitate distribution. The 2219Al alloy is a binary Al–Cu alloy that has a certain natural aging tendency. The most academically accepted aging precipitation sequence from the supersaturated solid solution (SSSS) is [27]: SSSS → GP zones → θ'' → θ' → θ. Figure 9 shows the bright-field TEM images of the BM, NZ, and LHZ on the 2219Al-T8 side of joints 2219RS-800-200 and 2219AS-800-200. For the 2219Al-T8 BM, the densely distributed plate-like precipitates 100 nm in length and 5–8 nm in thickness are believed to be metastable θ' (Al_2Cu) precipitates according to the previous studies [28–30] (Fig. 9a). However, only a few block-shaped equilibrium θ precipitates were observed in the NZ of joints 2219RS-800-200 and 2219AS-800-200 (Fig. 9b, d). Compared to those in the BM, coarser θ precipitates with a lower density were observed in the LHZ on the 2219Al-T8 side of joint 2219RS-800-200. Compared to that for joint 2219RS-800–200, θ precipitates of the LHZ on the 2219Al-T8 side showed larger size and lower density for joint 2219AS-800-200 (Fig. 9c, e).

The precipitates experienced a complex evolution process for FSW precipitation-hardened aluminum alloys under the varied welding parameters and material positions. It is necessary to discuss the precipitate evolution of the NZ and LHZ under various welding parameters before expounding the effect of material positioning.

Based on the precipitate observation in this study and Refs. [31, 32, 33], the relationship between the precipitates and microhardness is schematically shown in Fig. 10. During FSW, the original precipitates of the 2219Al-T8 BM simultaneously evolved in two ways, i.e., coarsening and dissolution. For the NZ, TMAZ, and HAZ of the FSW joint, the coarsening of precipitates during FSW was equivalent to the over aging (OA) of precipitates, resulting in lower hardness, whereas the natural aging (NA) taking place under room temperature condition for 7 days

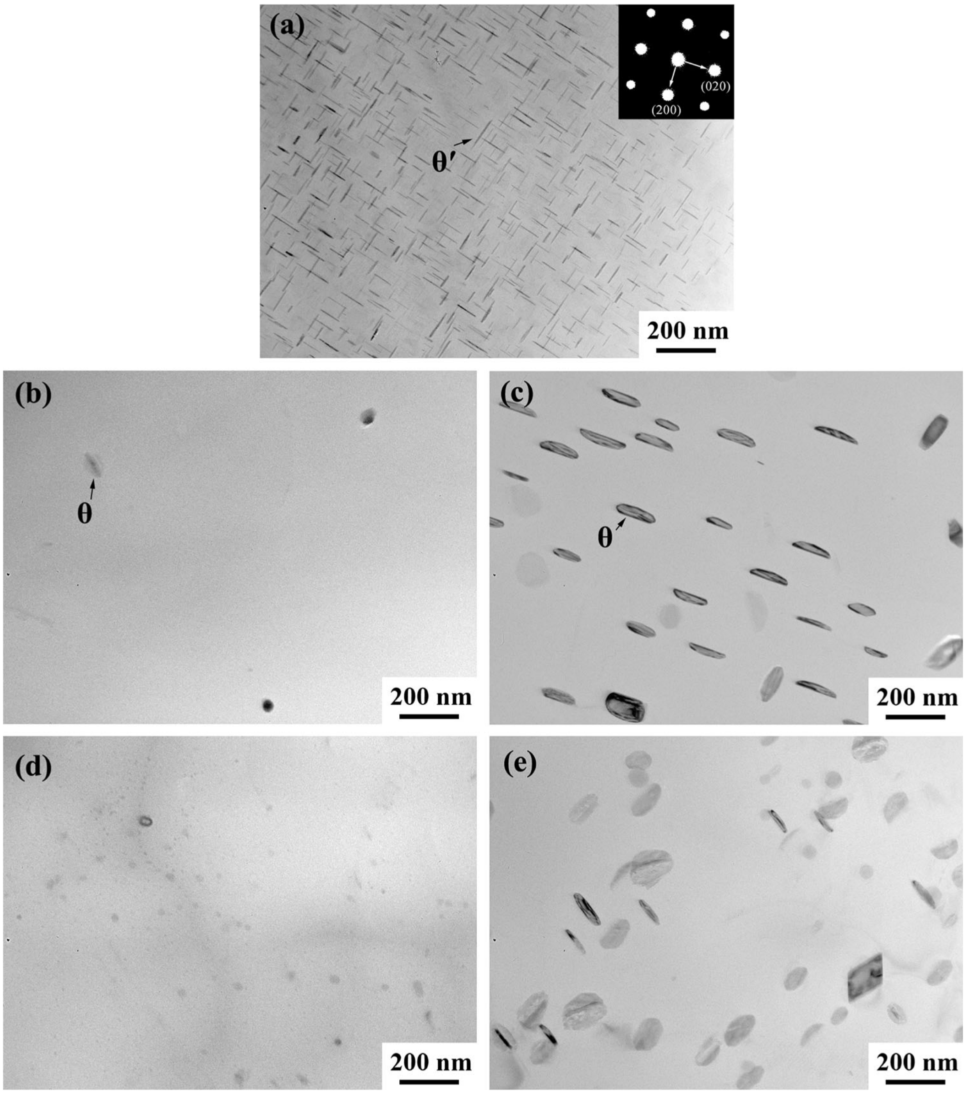

Figure 9 Precipitate distribution of **a** BM; **b** NZ and **c** LHZ on 2219Al-T8 side of joint 2219RS-800-200; **d** NZ and **e** LHZ on 2219Al-T8 side of joint 2219AS-800-200.

after FSW due to the dissolution of precipitates led to relative higher hardness. Thus, the precipitates of the FSW precipitation-hardened aluminum alloys could be divided into two kinds, i.e., NA precipitates and OA precipitates. The NA process resulted in the formation of two strengthening origins, i.e., Guinier–Preston (GP, present in the Al–Cu alloy)/Guinier–Preston–Bagaryatsky (GPB, present in the Al–Cu–Mg alloy) zones and a mass of solute clusters. Coarsened precipitates, such as Al_2Cu, Al_2CuMg, and $MgZn_2$, are produced during the OA process for varied precipitation-hardened aluminum alloys.

The NZ experienced severe plastic deformation and high heat input with a peak temperature of higher than 450 °C during FSW [34], resulting in the dissolution of most θ' precipitates and the transformation of the residual precipitates to the block-shaped equilibrium θ precipitates. This process was almost equivalent to solid solution heat treatment. Thus, only a few block-shaped equilibrium θ precipitates were observed in the NZ (Figs. 9b, d and 10a). During the subsequent NA process, GP zones were generally not formed in the NZ due to the slow heating and cooling processes of FSW as well as a weak NA tendency of 2219Al. It is highly probable that the solute clusters would form in the NZ, thereby resulting in the higher hardness of the NZ than that of the LHZs [17]. Thus, the microstructure evolution mechanism in the NZ of FSW precipitation-hardened aluminum alloys is characterized by the dissolution of most original precipitates and formation of NA precipitates (solute clusters).

The TMAZ and HAZ experienced the thermal circle with the peak temperature from 200 to 450 °C,

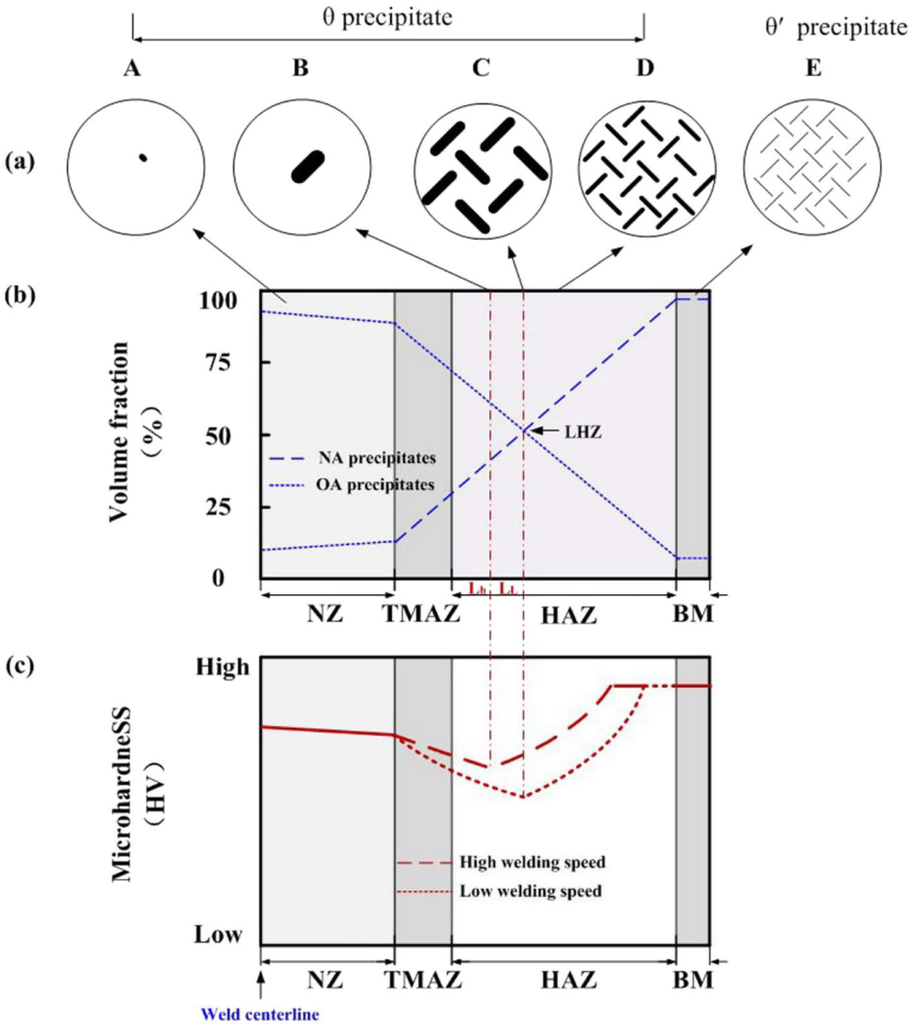

Figure 10 A schematic of microstructure evolution of FSW-hardened aluminum alloy, showing: **a** precipitate morphology, **b** evolution of NA precipitate and OA precipitate, and **c** microhardness distribution.

which corresponded to the overaging for precipitation-hardened aluminum alloys. According to the *Heat Source Zone-Isothermal Dissolution Layer* model proposed by Liu & Ma [14], the LHZs experienced thermal cycles with the similar peak temperature, which was 360–370 °C and 340 °C for FSW 6061Al-T6 joint [14] and FSW 2024Al-T351 joint [32], respectively. For FSW similar precipitation-hardened aluminum alloys, the softening of the LHZ is mainly determined by the welding speed and independent of the rotation rate [14, 32]. The LHZ of the FSW joints showed notably different precipitate morphology under the varied welding speeds.

The coarsening degree of Al_2Cu precipitates was mainly determined by the duration above the aging temperature of 190 °C, i.e., overaging time. The lower welding speed resulted in the longer overaging time and therefore resulted in high density of coarsened θ precipitates and the low hardness in the LHZ [18].

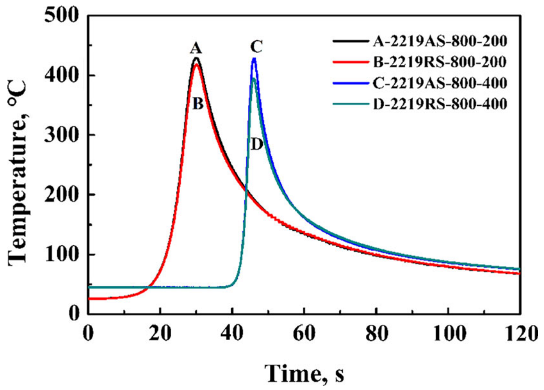

Figure 11 Temperature histories recorded at LHZs on 2219Al-T8 side of FSW 2219Al-T8/2195Al-T8 joints.

When increasing the welding speed, the shortened overaging time resulted in the lower density of θ precipitates and therefore the higher hardness in the LHZ (Fig. 10a–c).

The temperature histories during FSW recorded in the LHZs on the 2219Al-T8 side of joints 2219RS-800-200, 2219AS-800-200, 2219RS-800-400 and 2219AS-800-400 are shown in Fig. 11. Profiles A, B, C and D correspond to the thermal cycles of the LHZs on the 2219Al-T8 side for joints 2219AS-800-200, 2219RS-800-200, 2219AS-800-400 and 2219RS-800-400, respectively. Obviously, when 2219Al-T8 alloy was positioned on the AS, the LHZ on the 2219Al-T8 side experienced higher peak temperatures and therefore more dissolution of θ' precipitates than that on the RS (Fig. 9c, e). In this case, more solute cluster would form during the post-weld NA and higher hardness was therefore achieved in the LHZ on the 2219Al-T8 side of joints 2219AS-800-200 and 2219AS-800-400 (Figs. 5 and 6).

It is noted that the peak temperature of the LHZ on the 2219Al-T8 side about 400–430 °C in this study is higher than that of FSW 6061-T6 joint [14] and FSW 2024-T351 joint [32]. This may be related to that the LHZs of FSW 2219Al joint were more close to the weld center compared to FSW 6061Al-T6 joint and FSW 2024Al-T351 joint.

Tensile property, fracture location, and morphology

The tensile strength of the FSW 2219Al-T8/2195Al-T8 joints at RT and − 196 °C in this study and Ref. [13] is presented in Table 5, which reveals four important findings. Firstly, placing 2219Al-T8 on the AS resulted in higher tensile properties of the joints than that on the RS for the FSW joints under 800 rpm–200 mm min^{-1} and 800 rpm–400 mm min^{-1}. This is in agreement with the results of 6-mm-thick FSW 2219Al-T8/2195Al-T8 joint under 800 rpm–300 mm min^{-1} reported by Agilan et al. [13]. Secondly, for the identical material position with 2219Al-T8 on the RS or AS, the tensile strength of the FSW joints slightly increased with increasing the welding speed from 200 to 400 mm min^{-1}.

Thirdly, joints 2219AS-1200-800 and 2219AS-800-400 exhibited the nearly identical tensile strength. This may be associated with the property characters of FSW 2219-T8 joints. It was reported that the mechanical properties of FSW 2219Al-T8/2195Al-T8 joints are mainly determined by the LHZs on the 2219Al-T8 side [13], and the tensile strength of similar FSW 2219Al-T6 joints was independent of the rotation rate [14, 15]. This implied that the tensile strength of FSW 2219Al-T8/2195Al-T8 joint was independent of the rotation rate. The joint strength of similar FSW 2219Al-T6 joints increased by about 5–8 MPa with increasing the welding speed from 400 to 800 mm min^{-1} [16]. 2195Al alloy possessed higher strength and worse plastic deformation performance than 2219Al alloy. This would result in higher heat input in FSW 2219Al-T8/2195Al-T8 joint than that of similar FSW 2219Al-T6 joint, resulting in the nearly identical tensile strength for joints 2219AS-1200-800 and 2219AS-800-400. Thus, the tensile strength was essentially unchanged when the welding speed increased from 400 to 800 mm min^{-1} for the FSW 2219Al-T87/2195Al-T8 joints.

Fourthly, the FSW joints presented much higher tensile strength at − 196 °C than that at room temperature under the identical welding parameters and material position. This result is in agreement with the result reported by Agilan et al. [13]. The main reason

Table 5 Tensile properties of FSW 2219Al-T8/2195Al-T8 joints

Joint	Temperature, °C	Tensile properties		
		UTS, MPa	UTS$_{FSW}$/ UTS$_{BM}$, %	EI, %
2219RS-800-200	20	343 ± 3.3	74.3	6.6 ± 0.2
	− 196	435 ± 2.6	76.0	7.5 ± 0.1
2219RS-800-400	20	351 ± 0.6	75.9	6.8 ± 0.2
	− 196	444 ± 6.7	77.6	7.6 ± 0.3
2219AS-800-200	20	350 ± 0.8	75.8	6.9 ± 0.4
	− 196	444 ± 3.5	77.6	8.0 ± 0.2
2219AS-800-400	20	359.4 ± 8.5	77.8	6.7 ± 0.3
	− 196	454 ± 2.0	79.4	8.2 ± 0.1
2219AS-1200-800	20	358 ± 0.6	77.6	7.0 ± 0.2
2219AS-800-300 [13]	20	350	71.6	7.8
2219AS-800-300 [13]	20	367	75.1	8.5

is that the low temperatures enhanced the critical resolved shear stress by decreasing the equilibrium vacancy concentration and increasing dislocation motion resistance [35]. This suggested that the FSW 2219Al-T87/2195Al-T8 joint shows ideal services for low temperature fuel tanks.

It is noted that the changing trends of the joint strength with welding speed and material position of FSW 2219Al-T8/2195Al-T8 joints in this study are inconsistent with the results of Refs. [11, 12], which showed that placing 2219Al-T87 alloys on the AS or RS had no obvious effect on the tensile strength of the joint and the changing trends of the joint strength with welding speed are uncertain for the 2-mm-thick sound FSW 2219Al-T87/2195Al-T8 joints. The reason may be related with the thinning of the joint surface. During FSW, in order to avoid the welding defects, the tilt angle of the welding tool and the sufficient plunge depth were necessary and therefore resulted in the varied cross-sectional areas at various locations of the joints. This would undoubtedly influence the tensile properties and fracture locations of the FSW joints. The joint thinning exerted less influence on 6-mm-thick FSW 2219Al-T87/2195Al-T8 joints in Ref. [13], and this study but obviously affected the tensile properties and fracture behavior of 2-mm-thick FSW 2219Al-T87/2195Al-T8 joints in Refs. [11, 12]. By the joint surface planning, the FSW 2219Al-T87/2195Al-T8 joints exhibited an intrinsic joint strength and fracture locations in this study.

Figure 12 shows the fracture locations of the FSW joints under various welding parameters and material positions. All the joints fractured at the HAZs on the 2219Al-T8 side (Fig. 12a–d). The fracture path of the joints was along the LHZs on the 2219Al-T8 side and was about a ~ 45° to the tensile axis. Joint 2219AS-1200-800 showed the fracture location identical with that of joint 2219AS-800-400. Compared to that for the joints 2219RS-800-200 and 2219AS-800-200, the fracture locations significantly moved toward to the weld center and were still located at HAZ for joints 2219RS-800-400 and 2219AS-800-400 despite being very close to the HAZ (Fig. 12c, d). The similar fracture location was identified as the TMAZ for 6-mm FSW 2219Al-T8/2195Al-T8 joint under 800 rpm-300 mm min^{-1} in Ref. [13]. Moreover, different from the results in Ref. [13] and this study, the fracture location was affected by the joint thinning and was therefore located at the NZ or NZ/TMAZ interface for 2-mm-thick FSW 2219Al-T87/2195Al-T8 joints in Refs. [11, 12].

Figure 13 shows the intensity map of strain field recorded by digital correlation (DIC) during tension of joint 2219AS-800-200. It can be noted that a notable local necking occurred at the LHZ on the 2219Al-T8 side when $\sigma_s > 300$ MPa and no obvious plastic deformation was observed on the 2195Al-T8 side. This is consistent with the microhardness distribution as shown in Figs. 5 and 6. The necking became more obvious with increasing the stress. The maximum strain distribution coincided with the fracture location, which corresponded to the LHZ on the 2219Al-T8 side of the FSW joint. This result was in agreement with that of Ref. [36].

Figure 14 shows the typical SEM fractographs of joint 2219AS-800-200 at room temperature and − 196 °C. The macroscopic image of tensile fractured joints at room temperature shows a comparatively flat fracture surface (Fig. 14a). The microscopic image shows the transgranular fracture at position C (Fig. 14c). This is the typical fracture morphology for FSW precipitation-hardened aluminum alloys [14–17]. The macroscopic image of tensile fractured joints at − 196 °C shows a step-like fracture surface

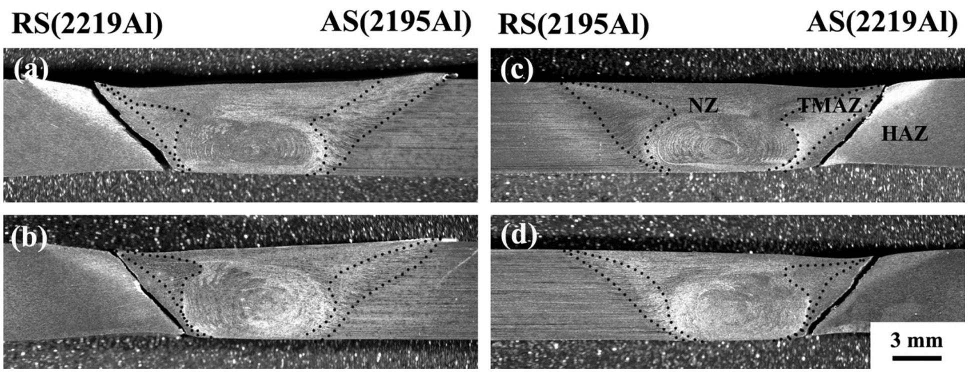

Figure 12 Fracture location of FSW 2219Al-T8/2195Al-T8 joints at 20 °C: **a** 2219RS-800-200, **b** 2219RS-800-400, **c** 2219AS-800-200, and **d** 2219AS-800-400.

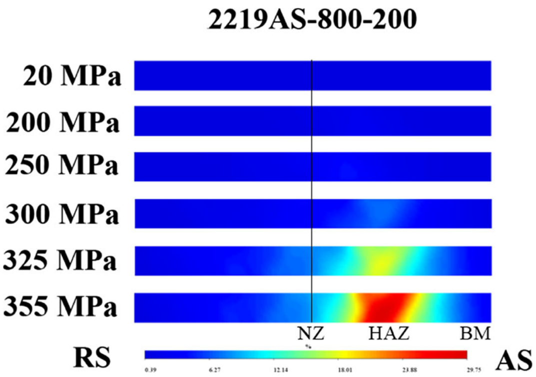

Figure 13 DIC tensile test showing local strain distribution of joint 2219AS-800-200.

(Fig. 14b). The microscopic image shows the fracture pattern with more toughness fracture characteristics at position D (Fig. 14d).

Bending performance

The bending failure angles of the FSW 2219Al-T8/2195Al-T8 joints under different welding parameters are shown in Table 6. It can be found that the up and down bending failure angles were about 91–117° and 88–109°, respectively. There is no clear correspondence relationship between the welding parameters, material positions and the bending failure angles.

Figure 15 shows the up and down bending failure locations of joints 2219AS-800-200 and 2219AS-1200-800. The cracking position of joint 2219AS-800-200 was located at the "S" line during up bending (marked with a white arrow in Fig. 15a, the magnified micrograph of which is shown in Fig. 15e) but was located at the HAZ on the 2195Al-T8 side during down bending (Fig. 15b). It should be noted that the up and down bending fracture locations of joints 2219RS-800-200, 2219RS-800-400, and 2219AS-800-400

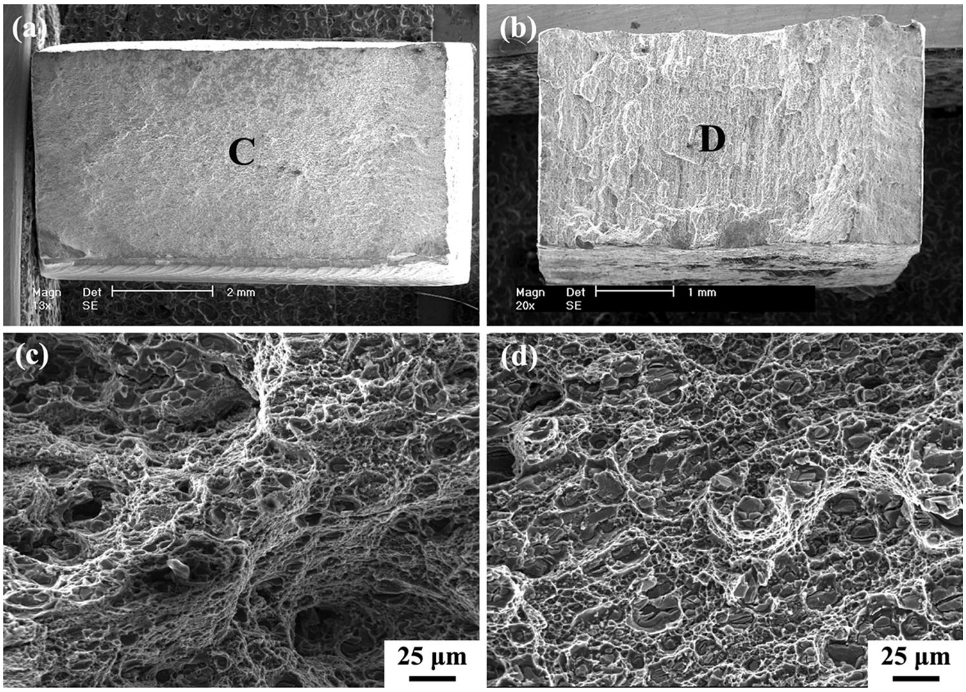

Figure 14 Fracture morphology of joint 2219AS-800-200: Macrographic fractographs at **a** 20 °C and **b** − 196 °C; magnified fractographs of specific positions in Fig. 13a, b: **c** position C and **d** position D.

Table 6 Bending failure angle (°) of FSW 2219Al-T8/2195Al-T8 joints

Joint	Up bending	Cracking location	Down bending	Cracking location
2219RS-800-200	98 ± 10.3	"S" line	104 ± 6.0	2195Al-T8-HAZ
2219RS-800-400	91 ± 3.8	"S" line	101 ± 3.9	2195Al-T8-HAZ
2219AS-800-200	111 ± 1.6	"S" line	88 ± 10.4	2195Al-T8-HAZ
2219AS-800-400	104 ± 10.0	"S" line	109 ± 5.7	2195Al-T8-HAZ
2219AS-1200-800	117 ± 5.3	"S" line	107 ± 6.2	"S" line

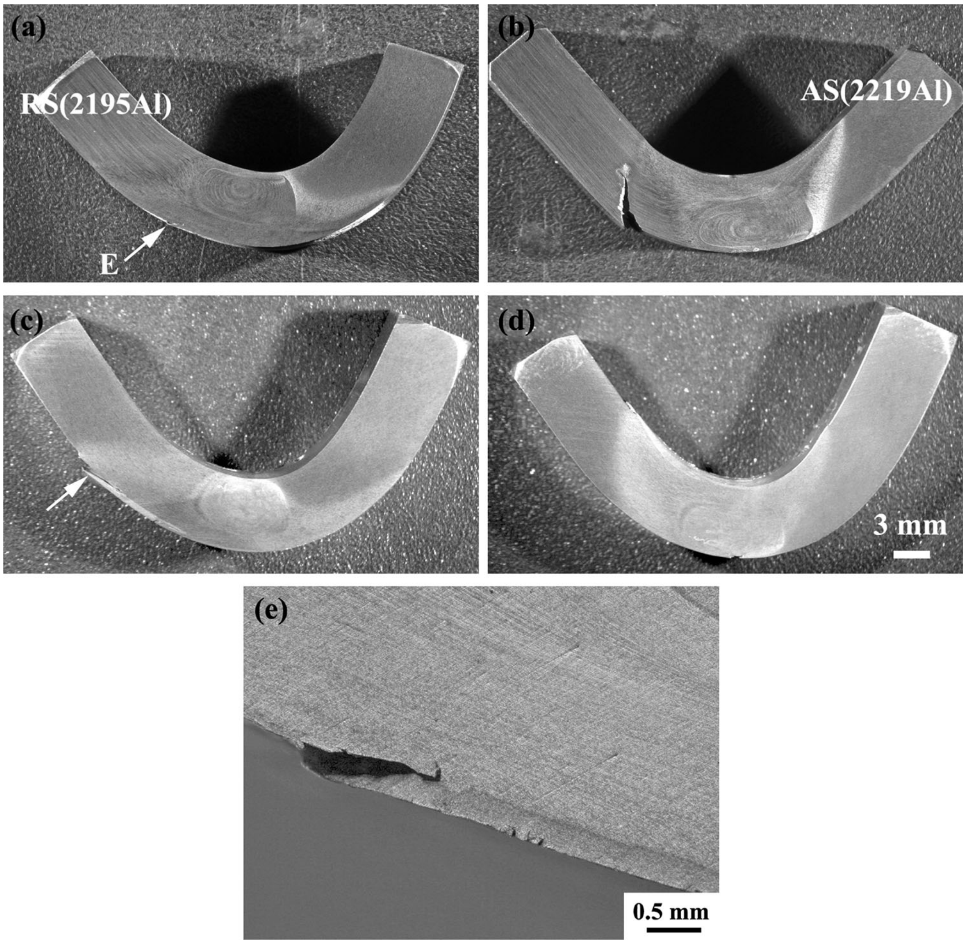

Figure 15 Bending fracture location of: **a** up bending and **b** down bending of joint 2219AS-800-200; **c** up bending and **d** down bending of joint 2219AS-1200-800; **e** the magnified micrograph of position E in **a**.

were identical to that of joint 2219AS-800-200. However, joint 2219AS-1200-800 fractured along “S” line during both up and down bending (Fig. 15c, d). The root “S” line was the weak zone during down bending, and less tortuous “S” line tended to preferentially crack at the bottom of the NZ [37]. The “S” line of joint 2219AS-1200-800 was much less tortuous than that of joint 2219AS-800-200 (Fig. 12c, e). Thus, the cracking position changed from the HAZ on the 2195Al-T8 side for joint 2219AS-800-200 to the “S” line for joint 2219AS-1200-800 during the down bending test.

The above results indicated that the “S” line and HAZ on the 2195Al-T8 side were the weak zones of FSW 2219Al-T8/2195Al-T8 joints during up and down bending tests. However, different from the results in this study, Xu et al. [38] reported that for the 6-mm-thick FSW 2219Al-T6 joint under 800–1300 rpm and 100–140 mm min^{-1}, no cracking was observed during the up bending but the cracking along the root of the “S” line occurred during the down bending. This suggested that 2195Al alloy exerted obvious influence on the bending performance of the FSW 2219Al-T8/2195Al-T8 joints.

Based on the results of this study, two considerations need to be emphasized for the applications of FSW 2219Al-T8/2195Al-T8 joints. Firstly, placing 2219Al-T8 alloy on the AS and welding speeds of 200–800 mm min^{-1} for rotation rates of 800–1200 rpm are advised to obtain the higher mechanical properties of the joints. Secondly, the “S” line or HAZ on the 2195Al-T8 side was the weak zone when the FSW 2219Al-T8/2195Al-T8 joints suffered from bending.

Conclusions

In this study, 6-mm-thick rolled 2219Al-T8 and 2195Al-T8 alloy plates were subjected to FSW under rotation rates of 800–1200 rpm at welding speeds of 200–800 mm min^{-1} with placing 2219Al-T8 alloy on the AS and RS, respectively. The microstructures, microhardness distribution, tensile and bending tests of the joints were carefully analyzed. The main conclusions and findings can be summarized as follows:

(1) The sound FSW 2219Al-T8/2195Al-T8 joints could be obtained under welding speeds of 200–800 mm min^{-1} for rotation rates of 800–1200 rpm despite the positioning of two alloys.

(2) The LHZ on the 2219Al-T8 side characterized by dissolution/coarsening of θ' precipitates always showed the lower hardness than that on the 2195Al-T8 side no matter which alloys were placed on the AS of the FSW 2219Al-T8/2195Al-T8 joints.

(3) When placing 2219Al-T8 alloy on the AS, the LHZ on the 2219Al-T8 side experienced higher peak temperature, and therefore more dissolution of θ' precipitates and more formation of solute clusters than that on the RS, thereby obtaining higher tensile strength.

(4) At room temperature and − 196 °C, the tensile strength of the FSW joints largely increased as the welding speed increased from 200 to 400 mm min^{-1}. The FSW joints presented much higher tensile strength at − 196 °C than that at room temperature. All the FSW joints fractured along the LHZs on the 2219Al-T8 side.

(5) The up and down bending failure angles of the FSW 2219Al-T8/2195Al-T8 joints were about 91–117° and 88–109°, respectively, with the weak zone appearing in the “S” line or HAZ on the 2195Al-T8 side.

Acknowledgements

This research is financially supported by (a) National Natural Science Foundation of China (No. 52275392); (b) the Youth Innovation Promotion Association of the Chinese Academy of Sciences (No. Y2021061); (c) Liaoning Province Excellent Youth Foundation (No. 2021–YQ–01); (d) Natural Science Foundation of Liaoning Province (No. 2021–MS–011); and (e) Joint Funds of the National Natural Science Foundation of China (U21B6004).

Author contributions

ZLW was involved in the experimental operation, data analysis and writing original draft. WLZ contributed to the resources, conception and design of this study. ZZ was involved in the experiment design, analysis, project administration, funding acquisition and writing original draft. BBW contributed to the experimental operation and data analysis. PX contributed to the funding acquisition, conception and design of this study. DRN contributed to the experimental conception, experimental design, supervision, writing and editing original draft. FCL contributed to the experimental conception and design. ZYM contributed to the oversight, writing and editing original draft. BLX contributed to the conception and design of this study. FFW and WDZ contributed to the resources and investigation.

Data availability

The data that support the findings of this study are available from the corresponding author upon reasonable request.

Declarations

Conflict of interest The authors declare that they have no known competing financial interests or personal relationships that could have appeared to influence the work reported in this paper.

References

[1] Xu WF, Liu JH, Luan GH, Dong CL (2009) Temperature evolution, microstructure and mechanical properties of friction stir welded thick 2219-O aluminum alloy joints. Mater Des 30(6):1886–1893. https://doi.org/10.1016/j.matdes.2008.09.021

[2] Wang G, Zhao Y, Hao Y (2018) Friction stir welding of high strength aerospace aluminum alloy and application in rocket tank manufacturing. J Mater Sci Technol 34(1):73–91. https://doi.org/10.1016/j.jmst.2017.11.041

[3] Rietz WW Jr (2009) Friction-stir welding–heavy inclusions in Bi-metallic welds of Al 2219/2195. In: 8th international conference on trends in welding research, pp 385–390. https://doi.org/10.1361/cp2008twr385

[4] Mishra RS, Ma ZY (2005) Friction stir welding and processing. Mater Sci Eng R 50(1–2):1–78. https://doi.org/10.1016/j.mser.2005.07.001

[5] Chen GQ, Yin QX, Zhang G, Zhang BG (2020) Fusion–diffusion electron beam welding of aluminum–lithium alloy with Cu nano–coating. Mater Des 188:108439. https://doi.org/10.1016/j.matdes.2019.108439

[6] Sharma C, Upadhyay V, Narwariya BS (2019) Tensile properties of dissimilar friction stir weld joints of Al–2024 and Al–7039 alloys. Mater. Res Express 6(2):026524. https://doi.org/10.1088/2053-1591/aaeca3

[7] Khodir SA, Shibayanagi T (2008) Friction stir welding of dissimilar AA2024 and AA7075 aluminum alloys. Mater Sci Eng B 148(1–3):82–87. https://doi.org/10.1016/j.mseb.2007.09.024

[8] Guo JF, Chen HC, Sun CN, Bi G, Sun Z, Wei J (2014) Friction stir welding of dissimilar materials between AA6061 and AA7075 Al alloys effects of process parameters. Mater Des 56:185–192. https://doi.org/10.1016/j.matdes.2013.10.082

[9] Daniolos NM, Pantelis DI (2017) Microstructural and mechanical properties of dissimilar friction stir welds between 6082–T6 and 7075–T651. Int J Adv Manuf Technol 88:2497–2505. https://doi.org/10.1007/s00170-016-8965-x

[10] Cavaliere P, De Santis AF, Squillace A (2009) Effect of welding parameters on mechanical and microstructural properties of dissimilar AA6082–AA2024 joints produced by friction stir welding. Mater Des 30(3):609–616. https://doi.org/10.1016/j.matdes.2008.05.044

[11] Fang Z, Wang F, Yin YH, Dong FB, Xu C, Zhang R, Chen K, Shan AD (2017) Microstructure and properties of 2195/2219 dissimilar alloy by FSW. Rare Metal Mater Eng 46(7):2017–2021

[12] Wang F, Fang Z, Xu C, Yin YH, Chen K (2015) Microstructure and mechanical properties of FSW joints between dissimilar high-strength aluminum alloys. J Aeronaut Mater 35(1):33–38

[13] Agilan M, Phanikumar G, Sivakumar D (2022) Tensile behaviour and microstructure evolution in friction stir welded 2195–2219 dissimilar aluminium alloy joints. Weld World 66:227–237. https://doi.org/10.1007/s40194-021-01217-w

[14] Liu FC, Ma ZY (2008) Influence of tool dimension and welding parameters on microstructure and mechanical properties of friction–stir–welded 6061–T651 aluminum alloy. Metall Mater Trans A 39:2378–2388. https://doi.org/10.1007/s11661-008-9586-2

[15] Ma ZY, Feng AH, Chen DL, Shen J (2018) Recent advances in friction stir welding/processing of aluminum alloys: microstructural evolution and mechanical properties. Crit Rev Solid State 43(4):269–333. https://doi.org/10.1080/10408436.2017.1358145

[16] Zhang Z, Xiao BL, Ma ZY (2012) Effect of welding parameters on microstructure and mechanical properties of friction stir welded 2219Al–T6 joints. J Mater Sci 47:4075–4086. https://doi.org/10.1016/j.matdes.2011.03.058

[17] Zhang Z, Xiao BL, Ma ZY (2015) Enhancing mechanical properties of friction stir welded 2219Al–T6 joints at high welding speed through water cooling and post-welding artificial ageing. Mater Character 106:255–265. https://doi.org/10.1016/j.matchar.2015.06.003

[18] Tao Y, Zhang Z, Yu BH, Xue P, Ni DR, Xiao BL, Ma ZY (2020) Friction stir welding of 2060–T8 Al Li alloy: Part I: microstructure evolution mechanism and mechanical properties. Mater Charact 168:110524. https://doi.org/10.1016/j.matchar.2020.110507

[19] Zhang J, Feng XS, Gao JS, Huang H, Ma ZQ, Guo LJ (2018) Effects of welding parameters and post-heat treatment on mechanical properties of friction stir welded AA2195-T8 Al-Li alloy. J Mater Sci Technol 34(1):219–227. https://doi.org/10.1016/j.jmst.2017.11.033

[20] Shu B, Guo XM, Zhang CX (2010) Microstructures and properties of friction stir welded joint of 2195 Al-Li alloy. J Aeronaut Mater 30(4):12–15

[21] Tao Y, Ni DR, Xiao BL, Ma ZY, Wu W, Zhang RX, Zeng YS (2017) Origin of unusual fracture in stirred zone for friction stir welded 2198–T8 Al-Li alloy joints. Mater Sci Eng A 693:1–13. https://doi.org/10.1016/j.msea.2017.03.079

[22] Das U, Toppo V (2018) Bending strength evaluation of dissimilar friction stir welded AA6101–T6 and AA6351–T65 aluminum alloys butt joint. Mater Today: Proc 5(5):11556–11562. https://doi.org/10.1016/j.matpr.2018.02.123

[23] Kang J, Si MY, Wang JJ, Zhou L, Jiao XD, Wu AP (2023) Effect of friction stir repair welding on microstructure and corrosion properties of 2219–T8 Al alloy joints. Mater Character 196:112634. https://doi.org/10.1016/j.matchar.2022.112634

[24] Bertrand R, Robe H, Texier D, Zedan Y, Feulvarch E, Bocher P (2019) Analysis of AA2XXX/AA7XXX friction stir welds. J Mater Process Technol 271:312–324. https://doi.org/10.1016/j.jmatprotec.2019.03.027

[25] Zhang Z, Xiao BL, Ma ZY (2013) Effect of segregation of secondary phase particles and "S" line on tensile fracture behavior of friction stir welded 2024Al–T351 joints. Metall Mater Trans A 44:4081–4097. https://doi.org/10.1007/s11661-013-1778-8

[26] Wang ZL, Zhang Z, Xue P, Ni DR, Ma ZY, Hao YF, Zhao YH, Wang GQ (2022) Defect formation, microstructure evolution, and mechanical properties of bobbin tool friction-

stir welded 2219–T8 alloy. Mater Sci Eng A 832:142414. https://doi.org/10.1016/j.msea.2021.142414

[27] Lorimer GW (1978) Precipitation Processes in Solids. TMS-AIME, Warrendale, Pa 121–160.

[28] Chen YC, Feng JC, Liu HJ (2009) Precipitate evolution in friction stir welding of 2219–T6 aluminum alloys. Mater Charact 60(6):476–481. https://doi.org/10.1016/j.matchar.2008.12.002

[29] Srinivasan PB, Arora KS, Dietzel W, Pandey S, Schaper MK (2010) Characterisation of microstructure, mechanical properties and corrosion behaviour of an AA2219 friction stir weldment. J Alloy Compd 492(1–2):631–637. https://doi.org/10.1016/j.jallcom.2009.11.198

[30] Paglia CS, Buchheit RG (2006) Microstructure microchemistry and environmental cracking susceptibility of friction stir welded 2219–T87. Mater Sci Eng A 49:107–114. https://doi.org/10.1016/j.msea.2006.05.036

[31] Genevois C, Deschamps A, Denquin A, Doisneau-cottignies B (2005) Quantitative investigation of precipitation and mechanical behaviour for AA2024 friction stir welds. Acta Mater 53(8):2447–2458. https://doi.org/10.1016/j.actamat.2005.02.007

[32] Zhang Z, Xiao BL, Ma ZY (2014) Hardness recovery mechanism in the heat-affected zone during long-term natural aging and its influence on the mechanical properties and fracture behavior of friction stir welded 2024Al-T351 joints. Acta Mater 73:227–239. https://doi.org/10.1016/j.actamat.2014.04.021

[33] Sato YS, Urata M, Kokawa H (2002) Parameters controlling microstructure and hardness during friction-stir welding of precipitation-hardenable aluminum alloy 6063. Metall Mater Trans A 33:625–635. https://doi.org/10.1007/s11661-002-0124-3

[34] Zhou L, Li GH, Liu CL (2017) Microstructural characteristics and mechanical properties of Al–Mg–Si alloy self-reacting friction stir welded joints. Sci Technol Weld Joi 22:438–445. https://doi.org/10.1080/13621718.2016.1251733

[35] Narayana GV (2006) Fracture behaviour of aluminum alloy AA 2219-T87 welded plates at room and cryo temperatures. Indian Institute of Technology Bombay

[36] Masoumi Khalilabad M, Zedan Y, Texier D, Jahazi M, Bocher P (2022) Effect of heat treatments on microstructural and mechanical characteristics of dissimilar friction stir welded 2198/2024 aluminum alloys. J Adhes Sci Technol 36(3):221–239. https://doi.org/10.1080/01694243.2021.1917868

[37] Sato YS, Takauchi H, Park SHC, Kokawa H (2005) Characteristics of the kissing-bond in friction stir welded Al alloy 1050. Mater Sci Eng A 405:333–338. https://doi.org/10.1016/j.msea.2005.06.008

[38] Xu WF, Liu JH, Luan GH, Dong CL (2009) Microstructure and mechanical properties of friction stir welded joints in 2219–T6 aluminum alloy. Mater Des 30:3460–3467. https://doi.org/10.1016/j.matdes.2009.03.018